Computers and Fluids 143 (2017) 59–72

Contents lists available at ScienceDirect

Computers and Fluids

journal homepage: www.elsevier.com/locate/compfluid

# Artificial viscosity model to mitigate numerical artefacts at fluid interfaces with surface tension

Fabian Denner[a,*], Fabien Evrard[a], Ricardo Serfaty[b], Berend G.M. van Wachem[a]

[a] Thermofluids Division, Department of Mechanical Engineering, Imperial College London, Exhibition Road, London, SW7 2AZ, United Kingdom
[b] PetroBras, CENPES, Cidade Universitária, Avenida 1, Quadra 7, Sala 2118, Ilha do Fundão, Rio de Janeiro, Brazil

ARTICLE INFO

*Article history:*
Received 21 April 2016
Revised 21 September 2016
Accepted 14 November 2016
Available online 15 November 2016

*Keywords:*
Capillary waves
Parasitic currents
Surface tension
Curvature
Interfacial flows

ABSTRACT

The numerical onset of parasitic and spurious artefacts in the vicinity of fluid interfaces with surface tension is an important and well-recognised problem with respect to the accuracy and numerical stability of interfacial flow simulations. Issues of particular interest are spurious capillary waves, which are spatially underresolved by the computational mesh yet impose very restrictive time-step requirements, as well as parasitic currents, typically the result of a numerically unbalanced curvature evaluation. We present an artificial viscosity model to mitigate numerical artefacts at surface-tension-dominated interfaces without adversely affecting the accuracy of the physical solution. The proposed methodology computes an additional interfacial shear stress term, including an interface viscosity, based on the local flow data and fluid properties that reduces the impact of numerical artefacts and dissipates underresolved small scale interface movements. Furthermore, the presented methodology can be readily applied to model surface shear viscosity, for instance to simulate the dissipative effect of surface-active substances adsorbed at the interface. The presented analysis of numerical test cases demonstrates the efficacy of the proposed methodology in diminishing the adverse impact of parasitic and spurious interfacial artefacts on the convergence and stability of the numerical solution algorithm as well as on the overall accuracy of the simulation results.



## 1. Introduction

The dynamics of an interface separating two immiscible fluids is governed by the behaviour of individual molecules, which typically have a size of less than one nanometer. Computational fluid dynamics (CFD), however, is based on continuum mechanics and treats fluids as continuous media. Molecular scales cannot be resolved using continuum mechanics, which leads to a variety of theoretical and numerical difficulties with respect to the representation of fluid interfaces using CFD. These difficulties manifest as parasitic (of unphysical origin) or spurious (of physical origin but numerically misrepresented) flow features in the vicinity of the interface. Numerical artefacts of particular practical interest in interfacial flow modelling that have attracted significant attention and research efforts are parasitic currents [1–7] and spurious capillary waves [1,8–13].

The numerical onset of unphysical flow currents in the vicinity of the interface, so-called *parasitic currents*, are a common occurrence in the modelling of surface-tension-dominated flows. Previous studies [3–6] have identified two distinct origins of parasitic currents: a) a discrete imbalance between pressure "jump" and surface tension and b) a numerically unbalanced evaluation of the interface curvature. The imbalance of the pressure gradient and surface tension can be eliminated by employing so-called balanced-force discretisation methods that assure a discrete balance between surface tension and pressure gradient, which has previously been proposed and successfully demonstrated by Renardy and Renardy [14] and Francois et al. [4] for sharp surface representations such as the ghost-fluid method [15,16], and by Francois et al. [4], Mencinger and Žun [5] and Denner and van Wachem [6] for methods using a continuum surface force formulation [1,17]. A numerically unbalanced evaluation of the interface curvature, which is typically associated with spatial aliasing errors resulting from the computation of the second derivative of a discrete indicator function or reconstruction [3,6], leads to an unphysical contribution to the momentum equations (via surface tension) and, consequently, causes an unphysical acceleration of the flow in the vicinity of the interface [4,7]. Using a balanced-force discretisation of the surface tension, parasitic currents are solely dependent

* Corresponding author:
*E-mail address:* fabian.denner@gmail.com (F. Denner).

http://dx.doi.org/10.1016/j.compfluid.2016.11.006

on the evaluation of the interface curvature and can, for instance, be eliminated (*i.e.* reduced to machine precision) for certain cases by imposing the geometrically exact curvature [4–7]. Although previous studies [7,18] have shown that, with a careful discretisation of the interface curvature, parasitic currents can be reduced to machine precision in some cases once the interface has reached a numerical equilibrium, parasitic currents are still an issue of significant practical relevance for applications with evolving interfaces, as evident by the considerable body of literature on this subject published over the past five years alone (*e.g.* [7,19–22]).

Another important numerical artefact in interfacial flows are *spurious capillary waves*. In a numerical framework, the shortest wavelength unambiguously resolved by the computational mesh is $\lambda_{\min} = 2\Delta x$, with $\Delta x$ representing the mesh spacing. Because an adequate spatial resolution of waves requires at least $6-10$ cells per wavelength [13], capillary waves with a wavelength of $\lambda_{\min} \leq \lambda \lesssim 3\lambda_{\min}$ are not part of the physical solution and can, therefore, be considered to be spurious capillary waves, meaning that these waves are a response of the discretised governing equations to a perturbation of the interface but are numerically misrepresented. Therefore, spurious capillary waves are, contrary to parasitic currents, not the result of numerical errors but the result of the limitations associated with the finite resolution of the computational mesh. The origin of spurious capillary waves can be physical perturbations of the interface, for instance due to the collision of the interface with an obstacle, as well as numerical perturbations, for instance the finite accuracy of numerical algorithms, discretisation errors or parasitic currents [13]. An adequate temporal resolution of the propagation of all spatially resolved capillary waves is essential for a stable numerical solution [1,13]. The dispersion relation of capillary waves in inviscid fluids is given as [23]

$$\omega_\sigma^2 = \frac{\sigma\, k^3}{\rho_\mathrm{a} + \rho_\mathrm{b}}\ , \tag{1}$$

from which the phase velocity follows as $c_\sigma = \omega_\sigma / k$, where $\omega_\sigma$ is the angular frequency of capillary waves, $k$ is the wavenumber, $\sigma$ is the surface tension coefficient and $\rho$ is the density of the adjacent fluids a and b. Hence, the phase speed of capillary waves increases with decreasing wavelength. This anomalously dispersive behaviour of capillary waves leads to a very rigid time-step restriction for interfacial flow simulations. For the shortest spatially resolved capillary waves, Denner and van Wachem [13] devised the capillary time-step constraint as

$$\Delta t_\sigma \leq \frac{\Delta x}{\sqrt{2}\, c_\sigma + u_\Sigma}\ , \tag{2}$$

where $\Delta x$ denotes the mesh spacing and $u_\Sigma$ is the flow velocity tangential to the interface. Denner and van Wachem [13] demonstrated that the shortest spatially resolved capillary waves are in most cases not subject to viscous attenuation, since the computational mesh is usually too coarse for typical values of the fluid viscosities to spatially resolve the vorticity generated by the shortest numerically represented waves.

The capillary time-step constraint limits the simulation of interfacial flow applications and has been commonly attributed to the explicit numerical implementation of surface tension. As a result, it is widely postulated that an implicit implementation of surface tension would lift or at least mitigate the capillary time-step constraint [1,8–10,18]. Recent research efforts inspired by this assumption aimed at finding an implicit or semi-implicit treatment of the surface tension to lift the time-step restrictions in interfacial flows [8,9,11,12]. Hysing [8] proposed a semi-implicit formulation of surface tension based on the CSF method [1] for a two-dimensional finite element method. The semi-implicit formulation of Hysing includes an additional implicit term which represents artificial shear stresses tangential to the interface. Raessi et al. [9] translated this methodology for finite volume methods and reported that this semi-implicit formulation of surface tension allows to exceed the capillary time-step constraint by up to factor five without destabilising the solution of the presented two-dimensional test cases. Schroeder et al. [11] proposed a two-dimensional method with a semi-implicit implementation of surface tension on a Lagrangian interface mesh (*i.e.* using an explicit representation of the interface) coupled to a Eulerian mesh for the flow, presenting stable results for time-steps up to $\Delta t = 3\,\Delta t_\sigma$. In a similar fashion, Zheng et al. [12] recently proposed a fully-implicit coupling of a Lagrangian interface mesh to a MAC grid and showed that the method can yield stable results for time-steps up to $\Delta t \approx 10^3\,\Delta t_\sigma$. However, with respect to methods that rely on an implicit interface representation, such as Volume-of-Fluid methods [24] or Level-Set methods [25,26], and the CSF method of Brackbill et al. [1], Denner and van Wachem [13] demonstrated that the temporal resolution requirements associated with the propagation of capillary waves is a result of the spatiotemporal sampling of capillary waves and is independent of whether surface tension is implemented explicit or implicit. Simulating the thermocapillary migration of a spherical drop, Denner and van Wachem [13] demonstrated that without external perturbations acting at the interface (such as parasitic currents), the capillary time-step constraint can be exceeded by several orders of magnitude without destabilising the solution, presenting stable results for $\Delta t = 10^4\,\Delta t_\sigma$ using an explicit implementation of surface tension. Thus, in order to mitigate or lift the capillary time-step constraint for numerical methods that rely on an implicit interface representation, the shortest capillary waves spatially resolved by the computational mesh have to be either filtered out or damped with an appropriate method to mitigate their impact.

Issues regarding numerical artefacts are, however, not limited to interfacial flows. For instance, numerical oscillations induced by a high-order discretisation of advection terms is a longstanding issue in CFD as well as numerical heat and mass transfer, and has been the topic of extensive studies, *e.g.* [27–31]. Artificial viscosity is a well-established concept to mitigate or eliminate high-frequency oscillations in the solution and improve the stability of the numerical methodology, in particular for shock capturing and in transsonic flows, and numerical models that incorporate artificial viscosity span a wide range of explicit and implicit methods, see *e.g.* [32–37]. Cook and Cabot [35] suggested that the artificial grid-dependent viscosity should be chosen as to only damp wavenumbers close to the Nyquist wavenumber $\pi/\Delta x$, which in a numerical simulation is the wavenumber of the shortest spatially resolved waves. Discretisation schemes which introduce numerical diffusion to avoid oscillatory solutions, such as TVD schemes [27–29], are often considered to be part of the artificial viscosity models as well. In fact, TVD schemes can be readily translated into an explicit artificial viscosity term, as for instance shown by Davis [38].

In this study we propose an artificial viscosity model to mitigate numerical artefacts at fluid interfaces, expanding on the work of Raessi et al. [9]. The proposed artificial viscosity model can accommodate arbitrary interface viscosities and two methods to dynamically compute the interface viscosity based on the local flow conditions are presented. We present and discuss the results for a range of numerical experiments, which allow a comprehensive assessment of the efficacy of the methodology, highlight the acting physical mechanisms and provide best practice guidelines for future interfacial flow simulations using the proposed artificial viscosity model. Furthermore, our study demonstrates that the success of the proposed methodology with regards to mitigating the capillary time-step constraint is solely based on the dissipation of surface energy, irrespective of the type of implementation, contrary to previous suggestions [8,9].

The remainder of this article is organised as follows. Section 2 introduces the governing equations and Section 3 presents the applied numerical framework. The artificial viscosity model is presented and appropriate choices of the interface viscosity as well as the acting physical mechanisms are discussed in Section 4. The results for a variety of numerical test cases are presented in Section 5, in order to scrutinise the proposed methodology, show its efficacy and provide a benchmark for future modelling efforts. The article is summarised and concluded in Section 6.

## 2. Governing equations

The considered isothermal, incompressible flow of Newtonian fluids is governed by the continuity equation and the momentum equations, defined as

$$\frac{\partial u_i}{\partial x_i} = 0 \tag{3}$$

$$\rho\left(\frac{\partial u_i}{\partial t} + u_j\frac{\partial u_i}{\partial x_j}\right) = -\frac{\partial p}{\partial x_i} + \frac{\partial}{\partial x_j}\left[\mu\left(\frac{\partial u_i}{\partial x_j} + \frac{\partial u_j}{\partial x_i}\right)\right] + \rho g_i + f_{s,i} \tag{4}$$

where $\boldsymbol{u}$ is the velocity, $p$ stands for the pressure, $\rho$ is the density, $\mu$ is the viscosity of the fluid, $t$ represents time, $\boldsymbol{g}$ is the gravitational acceleration and $\boldsymbol{f}_s$ is the volumetric force due to surface tension. Based on hydrodynamic principles, the forces acting on the interface must balance in both phases. Neglecting gradients in surface tension coefficient, the force-balance in the direction normal to the interface is [39]

$$p_b - p_a - \left(2\,\mu_b\frac{\partial(u_j\hat{m}_j)}{\partial x_i}\bigg|_b\hat{m}_i - 2\,\mu_a\frac{\partial(u_j\hat{m}_j)}{\partial x_i}\bigg|_a\hat{m}_i\right) = \sigma\,\kappa. \tag{5}$$

where subscripts a and b denote the two fluids, $\sigma$ is the surface tension coefficient, $\kappa$ is the interface curvature and $\hat{\boldsymbol{m}}$ is the unit normal vector of the interface (pointing into fluid b).

The Volume of Fluid (VOF) method [24] is adopted to capture the interface between two immiscible fluids. In the VOF method the local volume fraction in each cell is represented by the colour function $\gamma$, defined as

$$\gamma(\boldsymbol{x},t) = \begin{cases} 0 & \text{fluid a} \\ 1 & \text{fluid b.} \end{cases} \tag{6}$$

The interface is, therefore, situated in every mesh cell with a colour function value of $0 < \gamma < 1$. The local density $\rho$ and viscosity $\mu$ are defined based on the colour function $\gamma$, given as

$$\rho(\boldsymbol{x},t) = \rho_a\left[1-\gamma(\boldsymbol{x},t)\right] + \rho_b\,\gamma(\boldsymbol{x},t) \tag{7}$$

$$\mu(\boldsymbol{x},t) = \mu_a\left[1-\gamma(\boldsymbol{x},t)\right] + \mu_b\,\gamma(\boldsymbol{x},t)\ , \tag{8}$$

where subscripts $a$ and $b$ denote the two fluids. The advection of the colour function $\gamma$ is defined based on the underlying flow field as

$$\frac{\partial\gamma}{\partial t} + u_i\frac{\partial\gamma}{\partial x_i} = 0. \tag{9}$$

## 3. Numerical methodology

The applied numerical framework is based on a finite volume method with a collocated variable arrangement [6,40]. The transient term of the momentum equations, Eq. (4), is discretised using the Second-Order Backward Euler scheme and convection is discretised using a central differencing scheme. The continuity equation is discretised using a specifically constructed momentum-weighted interpolation method proposed by Denner and van Wachem [6], that couples pressure and velocity and assures a discrete balance between pressure gradient, gravity and surface force.

The solution procedure follows a coupled, implicit implementation of the primitive variables, following the work of Denner and van Wachem [6], where the governing equations of the flow are solved in a single linear system of equations, given as

$$\underbrace{\begin{pmatrix} x\text{-momentum equation} \\ y\text{-momentum equation} \\ z\text{-momentum equation} \\ \text{continuity equation} \end{pmatrix}}_{\boldsymbol{A}} \cdot \underbrace{\begin{pmatrix} \boldsymbol{\phi}_u \\ \boldsymbol{\phi}_v \\ \boldsymbol{\phi}_w \\ \boldsymbol{\phi}_p \end{pmatrix}}_{\boldsymbol{\phi}} = \boldsymbol{b}, \tag{10}$$

where $\boldsymbol{\phi}$ is the solution vector, constituted by the solution subvectors of velocity $\boldsymbol{u} = (u,v,w)^T$ and pressure $p$. Each time-step consists of a finite number of non-linear iterations to account for the non-linearity of the governing equations. At the end of each non-linear iteration the deferred terms of the equation system are updated, based on the result of the most recent non-linear iteration. This iterative procedure continues until the non-linear problem has converged to a sufficiently small tolerance. A BiCGSTAB method incorporated in the freely-available PETSc library [41,42] is utilised to solve the preconditioned linear equation system.

In this study a compressive VOF methodology [43] is applied to discretise the temporal evolution of the interface, governed by Eq. (9), using algebraic discretisation schemes to discretise Eq. (9) and transporting the colour function in a time-marching fashion. This compressive VOF methodology inherently conserves mass within the limits of the solver tolerance [43] and is able to capture evolving interfaces with similar accuracy as VOF-based interface reconstruction methods [43,44]. The interface advection and the flow solver are implemented in a segregated fashion and coupled explicitly, see Ref. [43] for details.

Based on the colour function distribution, the surface force per unit volume is discretised using the CSF model [1] as

$$f_{s,i} = \sigma\,\kappa\,\hat{m}_i\,\delta_\Sigma = \sigma\,\kappa\,\frac{\partial\gamma}{\partial x_i}\ , \tag{11}$$

where $\hat{\boldsymbol{m}} = \nabla\gamma/|\nabla\gamma|$ is the interface normal vector. In order to ensure a balanced-force discretisation of the surface force, Eq. (11) is discretised on the same computational stencil as the pressure gradient [6] and no convolution is applied to smooth the surface force [45].

## 4. Artificial viscosity model for interfacial flows

The assumption that an implicit treatment of surface tension can mitigate the capillary time-step constraint, first proposed by Brackbill et al. [1], has motivated recent efforts to formulate a (semi-)implicit implementation of the CSF model. Following the work of Bänsch [46], Hysing [8] proposed an additional implicit term for finite element methods that is dependent on the surface tension, which Raessi et al. [9] extended to finite volume methods, given as

$$f_{\tau,i} = \sigma\,\Delta t\,\delta_\Sigma\,\nabla_s^2 u_i\ , \tag{12}$$

where $\nabla_s^2$ is the Laplace-Beltrami operator tangential to the interface and $\delta_\Sigma = |\nabla\gamma|$ is the so-called interface density. The coefficient $\sigma\,\Delta t\,\delta_\Sigma$ of the tangential Laplacian of the velocity has the same unit (Pa s) as the dynamic viscosity $\mu$ and can, therefore, be seen as constituting an artificial interface viscosity. Consequently, the additional term given by Eq. (12) represents artificial shear stresses acting tangential to the interface in the interface region in addition to the shear stresses imposed by the bulk phases, increasing the dissipation of interface movement.

### 4.1. Artificial interfacial shear stresses

Following the analysis of Eq. (12) in the previous paragraph, the additional shear stresses acting tangential to the interface can be generalised as

$$f_{\tau,i} = \mu_\Sigma \, \nabla_s^2 u_i \ , \tag{13}$$

where $\mu_\Sigma$ is the interface viscosity, representing a numerical diffusion coefficient applied to smooth the topology of the fluid interface. For an isothermal, incompressible flow the momentum equations, Eq. (4), including the additional interfacial shear stress term of the artificial viscosity model become

$$\rho\left(\frac{\partial u_i}{\partial t} + u_j \frac{\partial u_i}{\partial x_j}\right) = -\frac{\partial p}{\partial x_i} + \frac{\partial}{\partial x_i}\left[\mu\left(\frac{\partial u_i}{\partial x_j} + \frac{\partial u_j}{\partial x_i}\right)\right] + \rho\, g_i + \sigma\, \kappa\, \frac{\partial \gamma}{\partial x_i} + \mu_\Sigma \, \nabla_s^2 u_i . \tag{14}$$

The prevailing effect of this additional interfacial shear stress term, Eq. (13), is an increased dissipation of surface energy through a local increase of the acting shear stresses. The underlying mechanism closely resembles the additional shear stresses imposed at the interface by the adsorption of surface-active substances, which in the literature is often described using a surface viscosity term, following the work of Scriven [47], that is identical to Eq. (13). With respect to surface-active substances the surface viscosity itself is, strictly speaking, not a fluid or interface property but should merely be regarded as a phenomenological constant [39]. The additional interfacial shear stress term, Eq. (13), also bears similarity to other types of artificial viscosity models, such as the original artificial viscosity model of von Neumann and Richtmyer [32] or the spectral-like artificial viscosity model of Cook and Cabot [35].

With respect to parasitic currents, the additional interfacial shear stresses play the traditional role of increasing the dissipation of parasitic currents, in particular since parasitic currents are spatially very localised and the associated second spatial derivatives are typically high. The effect of the additional interfacial shear stresses on spurious capillary waves is more versatile, as they reduce the frequency and phase velocity of capillary waves [48] and also increase the penetration depth of the vorticity induced by capillary waves [49], leading to (increased) attenuation of these waves. Furthermore, the increased viscosity acting on capillary waves steepens the energy cascade of capillary wave turbulence [50] and, thus, capillary waves with small wavelength that result from wave interaction are less energetic.

### 4.2. Choice of interface viscosity $\mu_\Sigma$

Defining an appropriate interface viscosity for a given problem is essential for the efficacy of the artificial viscosity model and the overall accuracy of the conducted simulation. If the interface viscosity is too small, parasitic and spurious artefacts cannot be counteracted with maximum effect. On the other hand, if the interface viscosity is too large, the artificial viscosity model compromises the predictive quality of the numerical framework and changes the outcome of the simulation. As a general template it is proposed to define the interface viscosity as

$$\mu_\Sigma = \mu_\Sigma^* \, \hat{\delta}_\Sigma \tag{15}$$

where $\mu_\Sigma^*$ is the base value of the interface viscosity, $\hat{\delta}_\Sigma = \delta_\Sigma \, \Delta x$ is the normalised interface density and $\Delta x$ is the mesh spacing. This formulation assures that the interface viscosity is non-zero only in the interface region as well as that the shear stress term of the artificial viscosity model is distributed in the same way as the force due to surface tension and, hence, only acts at the interface. As shown schmematically in Fig. 1, the normalised interface density is $0 \leq \hat{\delta}_\Sigma \leq 0.5$ and, hence, the applied interface viscosity in any given mesh cell is $\mu_\Sigma \leq 0.5\, \mu_\Sigma^*$. The base value of the interface viscosity can either be fixed to a predefined value or can be calculated based on the fluid properties and the flow field, such as the two specific examples discussed below.

The original formulation of the additional interfacial shear stress term proposed by Raessi et al. [9] is retained by defining the base value of the interface viscosity as

$$\mu_\Sigma^* = \frac{\sigma \, \Delta t}{\Delta x} . \tag{16}$$

This interface viscosity is proportional to the surface tension coefficient $\sigma$ and the time-step $\Delta t$ but inversely proportional to the mesh spacing $\Delta x$, similar to the magnitude of parasitic currents [4,6].

Denner and van Wachem [13] demonstrated that the viscous attenuation of interface waves in numerical simulations is critically influenced by the mesh resolution, concluding that the attenuation of spurious capillary waves cannot be represented in a physically accurate manner, since the vorticity generated by these waves is typically not discretely resolved by the computational mesh. Thus, an alternative definition of the interface viscosity is proposed based on the length scale of the penetration depth of the vorticity generated by capillary waves, given as [49]

$$l_\nu = \sqrt{\frac{\nu}{\omega_\sigma}} \ , \tag{17}$$

where $\nu = \mu/\rho$ is the kinematic viscosity. With respect to the dispersion of capillary waves, it can be assumed that the fluid properties of both phases act collectively on capillary waves [48], so that for instance the effective kinematic viscosity is $\nu = \nu_\mathrm{a} + \nu_\mathrm{b}$. Following this rational for the purpose of defining a length scale that takes into account the natural attenuation of capillary waves, for fluids with different fluid properties and including interface viscosity, this viscous length scale can be reformulated as

$$l_\nu = \sqrt{\frac{1}{\omega_\sigma}\left(\frac{\mu_\mathrm{a}}{\rho_\mathrm{a}} + \frac{\mu_\mathrm{b}}{\rho_\mathrm{b}} + \frac{\mu_\Sigma}{\rho_\Sigma}\right)} \ , \tag{18}$$

where $\rho_\Sigma = (\rho_\mathrm{a} + \rho_\mathrm{b})/2$ is the reference density at the interface. Hence, the base value of the interface viscosity follows as

$$\mu_\Sigma^* = \max\left\{\rho_\Sigma\left(l_\nu^2\, \omega_\sigma - \frac{\mu_\mathrm{a}}{\rho_\mathrm{a}} - \frac{\mu_\mathrm{b}}{\rho_\mathrm{b}}\right),\ 0\right\}. \tag{19}$$

This formulation of the interface viscosity takes into account the damping provided by the bulk phases as well as the increased attenuation of interface features with decreasing mesh spacing, since flow structures associated with parasitic currents and spurious capillary waves equally reduce in size. These flow structures experience a larger natural attenuation because viscosity acts preferably at smaller scales [23]. Furthermore, since underresolved interface waves are underdamped due to an inadequate resolution of the vorticity induced by these waves [13], a reduced mesh spacing (*i.e.* higher mesh resolution) increases the viscous dissipation of those waves. If the bulk phases provide sufficient damping, *e.g.* in the case of overdamped capillary waves [48], the interface viscosity becomes zero. Following the argument of Prosperetti [49], the viscous length scale in Eq. (19) is defined as $l_\nu = \Delta x$. Thus, the resulting interface viscosity leads to a penetration depth of the vorticity generated by an interfacial wave that is of the order of magnitude of the mesh spacing. The angular frequency $\omega_\sigma$ should be based on a representative wavelength, such as the minimum spatially resolved wavelength $\lambda_\mathrm{min} = 2\Delta x$ or the smallest wavelength that is spatially adequately resolved, *e.g.* $\lambda = 3\lambda_\mathrm{min} = 6\Delta x$. Note that this represents only one particular choice for the viscous length scale $l_\nu$ and the angular frequency $\omega_\sigma$ for Eq. (19) and that other choices may be more suitable for a given problem.

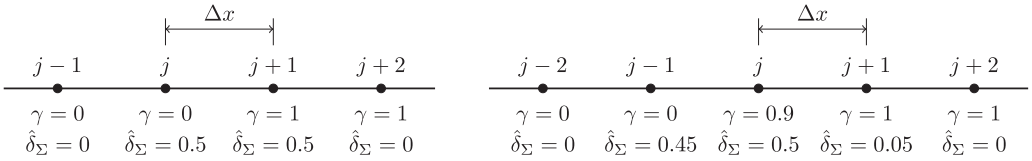


**Fig. 1.** One-dimensional examples of an equidistant Cartesian mesh with colour function $\gamma$ and corresponding normalised interface density $\hat{\delta}_\Sigma = |\nabla\gamma|\,\Delta x$, with $|\nabla\gamma_j| \approx |\gamma_{j+1} - \gamma_{j-1}|/(2\,\Delta x)$ discretised using central differencing.

The particular choice of interface viscosity also dominates the spatiotemporal convergence behaviour of the artificial viscosity model. The interface viscosity defined in Eq. (16) is $\mathcal{O}(\Delta x^{-1}, \Delta t)$. Thus, the interface viscosity diverges with first-order under mesh refinement, with $\mu^*_\Sigma = \infty$ for $\Delta x \to 0$, and converges with first-order for decreasing time-steps, with $\mu^*_\Sigma = 0$ for $\Delta t \to 0$. The interface viscosity defined in Eq. (19) with $l_\nu = \Delta x$, on the other hand, converges with order 0.5 for spatial refinement, since $\mu^*_\Sigma \propto \sqrt{\Delta x}$, and is independent of the time-step $\Delta t$.

### 4.3. Implementation

Hysing [8] and Raessi et al. [9] implemented Eq. (12) implicitly, assuming that an implicit implementation is required to lift the capillary time-step constraint. This widely advocated assumption has been corrected by Denner and van Wachem [13], demonstrating that restrictions imposed by the capillary time-step constraint also hold for the implicit implementation of surface tension. Contrary to previous studies [8,9], the additional interfacial shear stress term of the artificial viscosity model, Eq. (13), is implemented as an explicit contribution to the momentum equations, defined as

$$f^j_{\tau,i} = \mu_\Sigma\, \nabla_s^2 u_i^{j-1} \ , \tag{20}$$

where superscripts $j$ and $j-1$ denote the current and the previous non-linear iteration, respectively. The Laplace-Beltrami operator of velocity with respect to the tangential vector of the interface is

$$\nabla_s^2 u_i = \nabla \cdot \nabla_s u_i - (\hat{\boldsymbol{m}} \cdot \nabla)(\nabla_s u_i)\hat{\boldsymbol{m}} \ , \tag{21}$$

where

$$\nabla_s u_i = \nabla u_i - (\hat{\boldsymbol{m}} \cdot \nabla u_i)\hat{\boldsymbol{m}} \tag{22}$$

is the velocity gradient tangential to the interface.

Because the shear stress term of the artificial viscosity model is implemented explicitly, the applied time-step has to fulfil the viscous time-step constraint [9]

$$\Delta t_\mu \leq \frac{\rho\,\Delta x^2}{2\mu_\Sigma}. \tag{23}$$

Since the Cauchy stress tensor of the momentum equations, Eq. (4), is implemented implicity in the applied numerical framework, only the interface viscosity $\mu_\Sigma$ of the artificial viscosity model has to be considered in determining the viscous time-step constraint by Eq. (23). However, strict adherence to the viscous time-step constraint is in many cases not necessary, since the solution algorithm accounts iteratively for non-linearities of the governing equations and, hence, the additional interfacial shear stress term, Eq. (20), is changing in every iteration. Preliminary tests have shown that, with the numerical framework presented in Section 3, stability issues associated with the viscous time-step constraint only arise for very large interface viscosities.

Dependent on the mesh spacing, the fluid properties and the applied interface viscosity, the viscous time-step constraint $\Delta t_\mu$ can be more restrictive than the capillary time-step constraint $\Delta t_\sigma$, since $\Delta t_\mu \propto \Delta x^2$ and $\Delta t_\sigma \propto \Delta x^{3/2}$. Comparing $\Delta t_\mu$ and $\Delta t_\sigma$, the critical mesh spacing follows as

$$\Delta x_c = \frac{2\mu_\Sigma^2}{\pi\,\sigma\,\rho} \ , \tag{24}$$

and the largest stable time-step becomes

$$\Delta t_{\max} = \begin{cases} \Delta t_\sigma & \text{if } \Delta x > \Delta x_c \\ \Delta t_\mu & \text{if } \Delta x < \Delta x_c. \end{cases} \tag{25}$$

However, in many cases of practical interest $\Delta x \gg \Delta x_c$ with $\Delta t_\sigma \ll \Delta t_\mu$ and, hence, the viscous time-step constraint does not impose an additional limit to the applied time-step for such cases. The magnitude of capillary and viscous time-step constraints is further discussed for each individual test case in Section 5. An implicit implementation of $\nabla_s^2 \boldsymbol{u}$ and $\nabla_s \boldsymbol{u}$ [see Eqs. (21) and (22), respectively], as for instance described in detail by Raessi et al. [9], can remedy this issue for cases in which $\Delta t_\mu \ll \Delta t_\sigma$.

## 5. Results

The results of four representative test-cases are presented, scrutinising the proposed artificial viscosity model for interfacial flows by highlighting its acting mechanisms and discussing its impact on realistic applications. In what follows, $\mu^{*,t}_\Sigma$ denotes the interface viscosity based on the work of Hysing [8] and Raessi et al. [9], see Eq. (16), with superscript $t$ indicating its time-step dependency, and $\mu^{*,\lambda}_\Sigma$ denotes the interface viscosity determined by Eq. (19), where superscript $\lambda$ stands for its dependency on the chosen reference wavelength. For all presented simulations, the applied time-step satisfies the capillary time-step constraint, Eq. (2), the viscous time-step constraint, Eq. (23), as well as a Courant number $Co = |\boldsymbol{u}|\,\Delta t/\Delta x < 1$, unless explicitly stated otherwise.

### 5.1. Dispersion of capillary waves

A sinusoidal, surface-tension-driven wave between two viscous fluids is simulated. The wave with wavelength $\lambda$ has an initial amplitude of $0.01\lambda$ and the Laplace number of the two-fluid system is $La = \sigma\rho\lambda/\mu^2 = 3000$. Both fluids are initially at rest, have a density of $\rho = 1.0\,\mathrm{kg\,m^{-3}}$, a viscosity of $\mu = 1.6394 \times 10^{-3}\,\mathrm{Pa\,s}$ and a surface tension coefficient $\sigma = 0.25\,\pi^{-3}\,\mathrm{N\,m^{-1}}$, which results in a non-dimensional viscosity of

$$\epsilon = \frac{4\,\mu\,\pi^2}{\rho\,\omega_\sigma\,\lambda^2} = 6.472 \times 10^{-2}. \tag{26}$$

The motion of the interface is induced by surface tension only, gravity is excluded. The domain is $\lambda$ in width ($x$-direction) and $3\lambda$ in height ($y$-direction), identical to the domain used by Popinet [18], and is represented by an equidistant Cartesian mesh with a spatial resolution of 32 cells per wavelength $\lambda$. The periodic motion of the capillary wave is discretised with $\Delta t = 10^{-3}\,\mathrm{s}$ for $\lambda = 1\mathrm{m}$ and $\Delta t = 3.162 \times 10^{-5}\,\mathrm{s}$ for $\lambda = 0.1\mathrm{m}$, which corresponds to 1000 time-steps $\Delta t$ per period $\omega_\sigma^{-1}$. All domain boundaries are treated as free-slip walls. The capillary time-step constraint is $\Delta t_\sigma = 3.471 \times 10^{-2}\,\mathrm{s}$ for the wave with $\lambda = 1\,\mathrm{m}$ and $\Delta t_\sigma =$

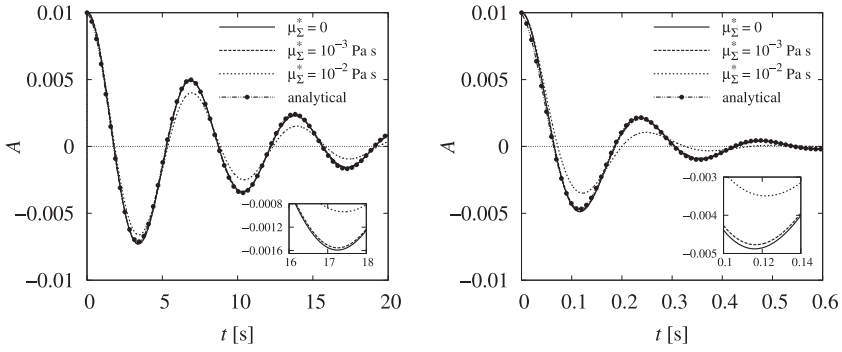


**Fig. 2.** Temporal evolution of the amplitude $A$ of the standing capillary wave with wavelength $\lambda = 1\,\mathrm{m}$ and $\lambda = 0.1\,\mathrm{m}$ for different interface viscosities $\mu^*_\Sigma$. The analytical result is based on the solution of the initial-value problem of Prosperetti [51].

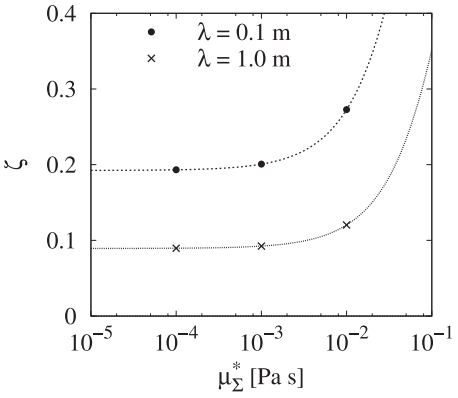


**Fig. 3.** Damping ratio $\zeta = \Gamma/\omega_0$ of the standing capillary wave with wavelength $\lambda = 1\,\mathrm{m}$ and $\lambda = 0.1\,\mathrm{m}$ for different interface viscosities $\mu^*_\Sigma$.

$1.098 \times 10^{-3}\,\mathrm{s}$ for $\lambda = 0.1\mathrm{m}$. Assuming $\mu^*_\Sigma = 10^{-2}\,\mathrm{Pa\,s}$, the viscous time-step constraint is $\Delta t_\mu = 1.953 \times 10^{-2}\,\mathrm{s}$ for $\lambda = 1\,\mathrm{m}$ and $1.953 \times 10^{-3}\,\mathrm{s}$ for $\lambda = 0.1\,\mathrm{m}$. Prosperetti [51] derived an analytical solution for the initial-value problem of the evolution of such a capillary wave in the limit of small wave amplitude and equal kinematic viscosity of the bulk phases.

Fig. 2 shows the temporal evolution of the amplitude for wavelengths $\lambda = 1\,\mathrm{m}$ and $\lambda = 0.1\,\mathrm{m}$ for the predefined interface viscosities $\mu^*_\Sigma = 0\,\mathrm{Pa\,s}$ (*i.e.* no artificial viscous shear stresses are applied at the interface), $\mu^*_\Sigma = 10^{-3}\,\mathrm{Pa\,s}$ and $\mu^*_\Sigma = 10^{-2}\,\mathrm{Pa\,s}$. The simulation results for both cases without artificial viscosity model ($\mu^*_\Sigma = 0$) are in excellent agreement with the analytical solution of Prosperetti [51], which is shown in the graphs as a reference. The temporal evolution of the amplitude of the capillary wave deviates increasingly from the analytical solution as the interface viscosity increases, due to the enhanced attenuation through the additional shear stresses imposed by the artificial viscosity model, given by the damping coefficient

$$\Gamma = \frac{\ln(|A_0|/|A_1|)}{t_1 - t_0}\,, \tag{27}$$

where $A$ is the wave amplitude, $t$ stands for time and superscripts 0 and 1 denote two extrema with respect to the temporal evolution of the wave amplitude. Fig. 3 shows the damping ratio $\zeta = \Gamma/\omega_\sigma$ of both waves as a function of interface viscosity. The damping ratio increases rapidly with increasing interface viscosity and, as previously indicated, the damping effect of the artificial viscosity model on the shorter wave ($\lambda = 0.1\,\mathrm{m}$) is significantly stronger.

The temporal evolution of the capillary wave amplitude $A$, with and without interface viscosity is shown in Fig. 4 for different mesh resolutions. Without interface viscosity ($\mu^*_\Sigma = 0$), see Fig. 4a, the prediction of the wave amplitude becomes more accurate, compared to the analytical results, with increasing mesh resolution. The results obtained on meshes with 64 cells and 128 cells per wavelength $\lambda$ are almost indistinguishable, indicating that a resolution of 64 cells per wavelength is sufficient. Applying the artificial viscosity model with $\mu^*_\Sigma = 10^{-2}\,\mathrm{Pa\,s}$, see Fig. 4b, the influence of the artificial viscosity model is diminishing with increasing mesh resolution. Since the artificial viscosity model is only applied in the close vicinity of the interface, the additional shear stresses introduced by the artificial viscosity model are acting in a region of decreasing volume for meshes with increasing resolution, thereby decreasing the added dissipation. The capillary and viscous time-step constraint for the case with 128 mesh cells per wavelength and $\mu^*_\Sigma = 10^{-2}\,\mathrm{Pa\,s}$ are $\Delta t_\sigma = 4.339 \times 10^{-3}\,\mathrm{s}$ and $\Delta t_\mu = 1.221 \times 10^{-2}\,\mathrm{s}$, respectively.

### 5.2. Interface instabilities on falling liquid films

Falling liquid films are convectively unstable to long-wave perturbations (*i.e.* the wavelength is much longer than the film height) which leads to the formation of periodic or quasi-periodic wave trains [52]. Waves with a frequency higher than the neutral stability frequency $f_{\mathrm{crit}}$ are attenuated by surface tension, whereas waves with a frequency lower than $f_{\mathrm{crit}}$ evolve as a result of the long-wave instability mechanism [53]. The resulting solitary waves are governed by complex hydrodynamic phenomena and exhibit a dominant elevation with a long tail and steep front, typically with capillary ripples preceding the main wave hump. In inertia-dominated film flows, solitary waves exhibit a separation of scales between the front of the main wave hump, where gravity, viscous drag and surface tension balance, and the tail of the wave, characterised by a balance between gravity, viscous drag and inertia [52].

Two different film flows are considered to study the effect of the artificial viscosity model: a) the attenuation of numerical artefacts at the interface, and b) the spatiotemporal aliasing of spurious capillary waves. Both cases are simulated in a domain of size $L_x \times L_y \times 0.1h_\mathrm{N}$, schematically illustrated in Fig. 5, represented by an equidistant Cartesian mesh with 10 cells per film height $h_\mathrm{N}$, where $h_\mathrm{N}$ is the height of the unperturbed film (Nusselt height) for a given flow rate according to the Nusselt flat film solution [52]. For all cases considered in this study the domain height is $L_y = 4h_\mathrm{N}$. The inclined substrate has an inclination angle $\beta$ to the horizontal plane and is modelled as a no-slip boundary. The gas-side (top) boundary is assumed a free-slip wall. A monochromatic perturbation is imposed at the domain-inlet, periodically changing

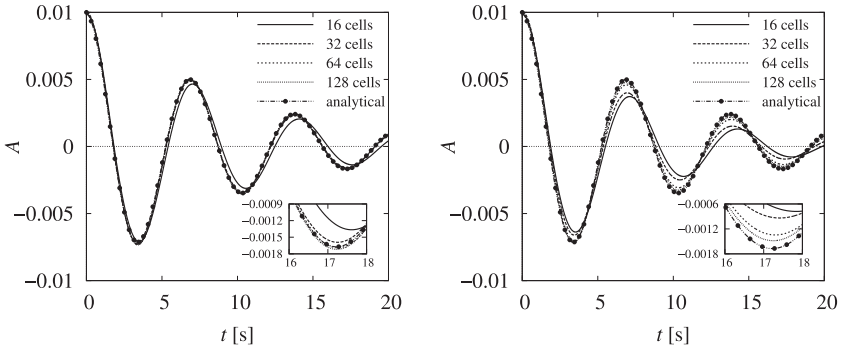


(a) $\mu_\Sigma^* = 0$ (b) $\mu_\Sigma^* = 10^{-2}$ Pa s

**Fig. 4.** Temporal evolution of the amplitude $A$ of the standing capillary wave with wavelength $\lambda = 1$ m and interface viscosities $\mu_\Sigma^* = 0$ and $\mu_\Sigma^* = 10^{-2}$ Pa s for different mesh resolutions, indicated by the number of cells per wavelength $\lambda$. The analytical result is based on the solution of the initial-value problem of Prosperetti [51].

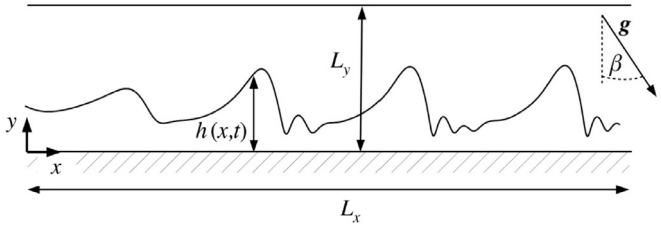


**Fig. 5.** Schematic illustration of the numerical domain with dimensions $L_x \times L_y$. The liquid film with height $h(x, t)$ flows from left to right on substrate with inclination angle $\beta$.

the mass flow at frequency $f$ and amplitude $A$ from the mean, with a semi-parabolic velocity profile prescribed for the liquid phase at the inlet

$$u(x = 0,\ 0 \le y \le h_\mathrm{N}) = \frac{3}{2}[1 + A\ \sin(2\pi f t)]\left(2\,\frac{y}{h_\mathrm{N}} - \frac{y^2}{h_\mathrm{N}^2}\right)u_\mathrm{N}\ , \tag{28}$$

and a spatially-invariant velocity prescribed at the inlet for the gas-phase

$$u(x = 0,\ h_\mathrm{N} < y \le 4h_\mathrm{N}) = \frac{3}{2}[1 + A\ \sin(2\pi f t)]u_\mathrm{N}\ , \tag{29}$$

where $u_\mathrm{N}$ is mean flow velocity (Nusselt velocity) based on the Nusselt flat film solution [52], given as

$$u_\mathrm{N} = \frac{\rho_\mathrm{l} g \sin\beta\, h_\mathrm{N}^2}{3\,\mu_\mathrm{l}}. \tag{30}$$

The film height $h(x = 0) = h_\mathrm{N}$ at the inlet is constant and an open boundary condition is applied at the domain-outlet [54,55]. The film is initially flat and the velocity field is fully developed.

*5.2.1. Mitigating parasitic currents*

Following the work of Denner et al. [56] and Charogiannis et al. [57], the considered liquid film has a Reynolds number of $Re = \rho_\mathrm{l} u_\mathrm{N} h_\mathrm{N}/\mu_\mathrm{l} = 20.55$ and is flowing down a substrate with an inclination angle of $\beta = 20^\circ$ to the horizontal. The liquid phase has a density of $\rho_\mathrm{l} = 1169.165\,\mathrm{kg\,m^{-3}}$ and a viscosity of $\mu_\mathrm{l} = 1.8433 \times 10^{-2}$ Pa s, the gas phase has a density of $\rho_\mathrm{g} = 1.205\,\mathrm{kg\,m^{-3}}$ and a viscosity of $\mu_\mathrm{g} = 1.82 \times 10^{-5}$ Pa s, and the surface tension coefficient is $\sigma = 5.8729 \times 10^{-2}\,\mathrm{N\,m^{-1}}$. The Nusselt height for this film flow is $h_\mathrm{N} = 1.65923 \times 10^{-3}$ m and the Nusselt velocity is $u_\mathrm{N} = 1.95296 \times 10^{-1}\,\mathrm{m\,s^{-1}}$. The length of the applied three-dimensional domain is $L_x = 205 h_\mathrm{N}$ and the perturbation frequency is $f = 7\,\mathrm{s^{-1}}$ with an amplitude of $A = 11.38\%$. The capillary time-step constraint for this case is $\Delta t_\sigma = 9.927 \times 10^{-5}$ s, whereas the viscous time-step constraint is $\Delta t_\mu = 9.965 \times 10^{-4}$ s for $\mu_\Sigma^* = \mu_\Sigma^{*,t}$ and $\Delta t_\mu = 1.163 \times 10^{-4}$ s for $\mu_\Sigma^* = \mu_\Sigma^{*,\lambda}$.

Fig. 6a shows the film height $h$, normalised by the Nusselt flat film height $h_\mathrm{N}$, and Fig. 6b shows the streamwise velocity at the interface $u_\Sigma$, normalised by the Nusselt velocity $u_\mathrm{N}$, as a function of the normalised downstream distance $x$. Experimental results for this particular case of Denner et al. [56] are shown as a reference. The impact of numerical artefacts at the front of the solitary wave is clearly visible in Fig. 6, manifesting as wiggles of the film height $h$ (see inset of Fig. 6a), particularly between the wave crest and the preceding trough, and as strong fluctuations of the interface velocity $u_\Sigma$ (see inset of Fig. 6b). Since the applied time-step satisfies $\Delta t_\sigma$, no external perturbations of high frequency are applied and given that the numerical artefacts occur in a region of relatively high curvature and low shear stress, the observed numerical artefacts are most likely parasitic currents. No such wiggles and fluctuations are observed if the artificial viscosity model is applied with either of the two considered definitions of the interface viscosity. However, the artificial viscosity model noticeably influences the hydrodynamics of the capillary ripple preceding the solitary wave. With increasing interface viscosity ($\mu_\Sigma^{*,t} = 0.0334$ Pa s and $\mu_\Sigma^{*,\lambda} = 0.277$ Pa s) the amplitude of the capillary ripple preceding the solitary wave is considerably reduced and its wavelength is increased, leading to smaller variations in interface velocity. Capillary ripples form in order for the surface energy of the interface to balance the inertia of the flow and an increasing number of capillary ripples is generally observed for increasing inertia [52,58]. As a consequence of the artificial viscosity model increasing the dissipation in the vicinity of the interface (which is acting particularly at short wavelengths [48]) and, therefore, dissipating some of the inertia of the flow, the resulting capillary ripple is smaller for increasing interface viscosity.

*5.2.2. Spatiotemporal aliasing of spurious capillary waves*

Since the interface and the flow field are clearly oriented, falling liquid films are well suited to study the onset of spatiotemporal aliasing of spurious capillary waves as a result of breaching the capillary time-step constraint given in Eq. (2), as demonstrated by Denner and van Wachem [13]. Spurious capillary waves have typically a frequency that is significantly larger than the neutral stability frequency $f_\mathrm{crit}$ and, hence, from a purely physical viewpoint, spurious capillary waves should be naturally attenuated. Raessi et al. [9] reported that an implicit implementation of the additional interfacial shear stress term, Eq. (12), allowed them to conduct numerically stable simulation with time-steps up to 5 times larger than the capillary time-step constraint of Brackbill et al. [1].

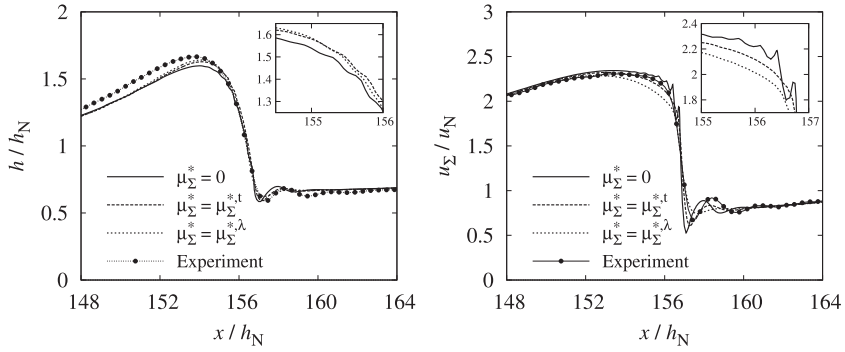


(a) Film height $h$ (b) Interface velocity $u_\Sigma$

**Fig. 6.** Film height $h$, normalised with the Nusselt film height $h_N$, and streamwise velocity at the interface $u_\Sigma$, normalised with the Nusselt velocity $u_N$, as a function of normalised downstream distance $x$. The insets show a magnified view of the front of the main wave hump, which is visibly affected by parasitic currents. The corresponding reference interface viscosities are $\mu_\Sigma^{*,t} = 3.34 \times 10^{-2}$ Pa s and $\mu_\Sigma^{*,\lambda} = 2.77 \times 10^{-1}$ Pa s. Experimental results of Denner et al. [56] are shown as a reference.

As previously discussed in the introduction of this article, Hysing [8] as well as Raessi et al. [9] attributed this behaviour to the implicit implementation of this term, a hypothesis which has later been disputed by Denner and van Wachem [13]. In the current study the additional shear stress term of the artificial viscosity model, Eq. (13), is implemented explicitly, as detailed in Section 4.3.

A falling water film on a vertical ($\beta = 90°$) substrate is simulated, as previously considered experimentally and numerically by Nosoko and co-workers [54,59]. The liquid phase has a density of $\rho_l = 998\,\mathrm{kg\,m^{-3}}$ and a viscosity of $\mu_l = 10^{-3}$ Pa s, whereas the gas phase is taken to have a density of $\rho_g = 1.205\,\mathrm{kg\,m^{-3}}$ and a viscosity of $\mu_g = 10^{-5}$ Pa s. The surface tension coefficient is $\sigma = 7.2205 \times 10^{-2}\,\mathrm{N\,m^{-1}}$. The liquid film flow has a Reynolds number of $Re = 51.1$ with $h_N = 2.51 \times 10^{-4}$ m. The computational domain has a length of $L_x = 300 h_N$ and the perturbation frequency is $f = 25\,\mathrm{s^{-1}}$ with an amplitude of $A = 3\%$. Given the neutral stability frequency for this case is $f_{crit} = 169.3\,\mathrm{s^{-1}}$, the shortest spatially resolved capillary waves with $\lambda_{min} = 2\Delta x$ and $f(\lambda_{min}) = 59.9 \times 10^3\,\mathrm{s^{-1}}$ are naturally attenuated and, hence, any observed growth of these waves is a numerical artefact.

Fig. 7a and b shows the film height as a function of downstream distance of the falling water film at two time instants for different numerical time-steps. The capillary time-step constraint following Eq. (2) is $\Delta t_\sigma = 5.52 \times 10^{-6}$ s, assuming $\boldsymbol{u}_\Sigma \cdot \boldsymbol{k} = 1.5\,u_N$ (which is the streamwise interface velocity of the unperturbed film). In Fig. 7a the onset of spatial aliasing for the case with $\Delta t = 8.31 \times 10^{-6}$ s and $\mu_\Sigma^* = 0$ is starting to be visible, even in the flat section of the film for $x \gtrsim 160\,h_N$, while the other two cases do not exhibit any aliasing. The aliasing severely influences the evolution of the falling liquid film shortly after its onset, see Fig. 7b, in particular at the crest and the preceding trough of the largest interfacial wave. No aliasing is observed if the time-step is reduced to satisfy the capillary time-step constraint ($\Delta t < \Delta t_\sigma$), exemplified by the case with $\Delta t = 3.92 \times 10^{-6}\,\mathrm{s} \approx 0.71\,\Delta t_\sigma$ in Fig. 7. Applying the artificial viscosity model with $\mu_\Sigma^* = \mu_\Sigma^{*,t} = 0.0239$ Pa s, for which $\Delta t_\mu = 2.634 \times 10^{-5}$ s applies, increases the dissipation of the surface energy of spurious capillary waves and, even with $\Delta t = 8.31 \times 10^{-6}\,\mathrm{s} \approx 1.5\,\Delta t_\sigma$, results in a smooth and accurate evolution of the interface without aliasing. Note that the interface viscosity is 23.9 times larger than the viscosity of the liquid and is, therefore, increasing the penetration depth of the vorticity generated by capillary waves, see Eq. (17), by almost factor 5. This leads to a significantly increased attenuation of spurious capillary waves, which is essential for the ability to breach the capillary time-step constraint $\Delta t_\sigma$. It is possible to apply a larger time-step than in the shown example but this would generally require a larger interface viscosity and would, therefore, have a more pronounced impact on the accuracy of the simulation results. It is worth noting that despite the explicit implementation of the artificial viscosity model, the numerical algorithm is stable and spurious capillary waves are

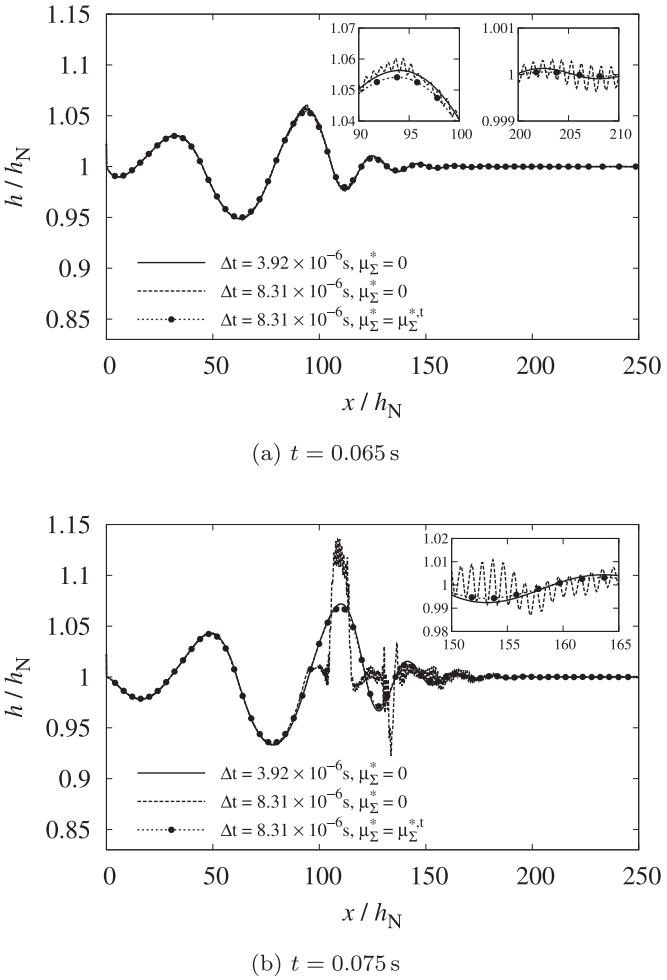


(a) $t = 0.065$ s

(b) $t = 0.075$ s

**Fig. 7.** Film height $h$, normalised with the Nusselt film height $h_N$, as a function of normalised downstream distance $x$ of the vertically falling water film with perturbation frequency $f = 25\,\mathrm{s^{-1}}$ at (a) time $t = 0.065$ s and (b) $t = 0.075$ s for different time-steps $\Delta t$. The insets show magnified views of the film height at specific downstream distances. The reference interface viscosity is $\mu_\Sigma^{*,t} = 0.0239$ Pa s and the capillary time-step constraint is $\Delta t_\sigma = 5.52 \times 10^{-6}$ s.

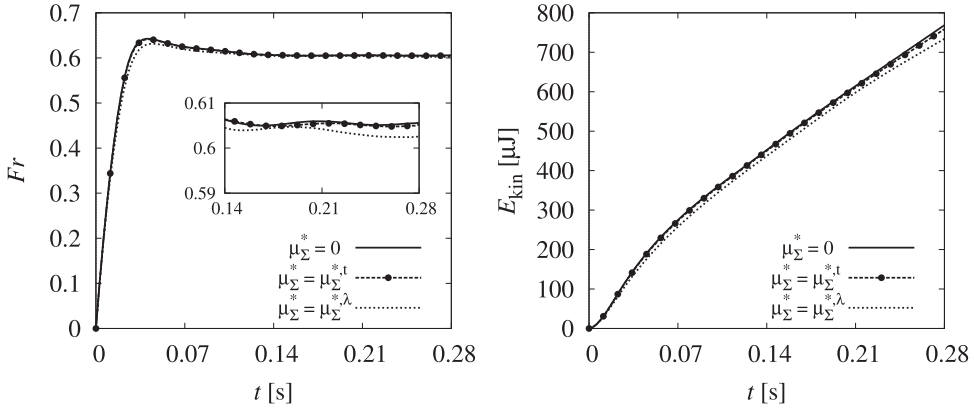


(a) Froude number $Fr$ (b) Total kinetic energy $E_{\mathrm{kin}}$

**Fig. 8.** Temporal evolution of (a) the Froude number $Fr$ and (b) the total kinetic energy $E_{\mathrm{kin}} = \rho \boldsymbol{u}^2/2$ in the computational domain of the rising bubble with $Eo = 40$ and $Mo = 0.056$.

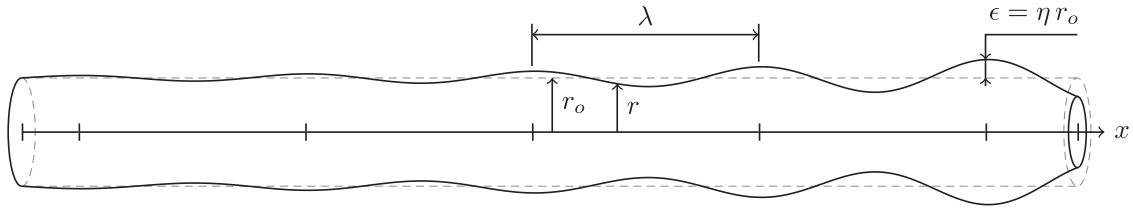


**Fig. 9.** Capillary instability with wavelength $\lambda$ and amplitude $\eta$ on a liquid jet with radius $r$ and initial radius $r_0$.

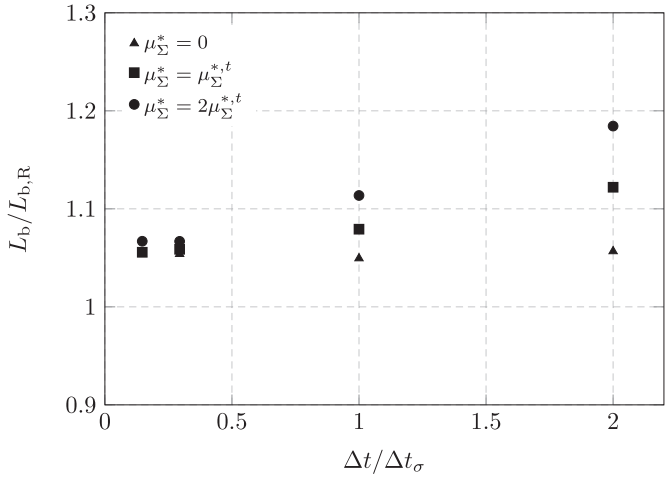


**Fig. 10.** Comparison of the numerical breakup length $L_b$ and the theoretical breakup length $L_{b,R}$ based on the linear stability analysis of Rayleigh [63] for different interface viscosities $\mu^*_\Sigma$ and for different time-steps $\Delta t$.

not amplified, allowing to breach the capillary time-step constraint without consequences.

### 5.3. Buoyancy-driven rise of a bubble

The rise of a bubble due to the sole action of buoyancy, characterised by its Morton number $Mo = g\,\mu_o^4/\rho_o\,\sigma^3 = 0.056$ and its Eötvös number $Eo_d = \rho_o\, g\, d_0^2/\sigma = 40$ is simulated and analysed. The continuous phase has a density of $\rho_o = 1000\,\mathrm{kg\,m^{-3}}$ and a viscosity of $\mu_o = 0.2736\,\mathrm{Pa\,s}$. Following previous studies [6,43,44,60], the density and viscosity ratio of the bubble are $\rho_i/\rho_o = \mu_i/\mu_o = 10^{-2}$. The bubble is initially spherical with a diameter of $d_0 = 0.02\,\mathrm{m}$, the surface tension coefficient is $\sigma = 0.1\,\mathrm{N\,m^{-1}}$ and the gravitational acceleration of $g = 10\,\mathrm{m\,s^{-2}}$ is acting in negative $y$-direction. Both fluids are initially at rest and the motion of the bubble is induced by buoyancy only. The applied computational domain has a size of $5d_0 \times 7d_0 \times 5d_0$ and is resolved with an equidistant Cartesian mesh of $100 \times 140 \times 100$ cells. The boundary at the top of the domain is considered to be an outlet boundary, all other boundaries are free-slip walls. Given the domain width of $5d_0$, the rise velocity in the applied computational domain is expected to be 96% of the rise velocity observed in a domain of infinite extend [6]. The capillary time-step constraint is $\Delta t_\sigma = 9.185 \times 10^{-4}\,\mathrm{s}$ and the viscous time-step constraint is $\Delta t_\mu = 1.143 \times 10^{-2}\,\mathrm{s}$ for $\mu^*_\Sigma = \mu^{*,t}_\Sigma$ and $\Delta t_\mu = 1.660 \times 10^{-3}\,\mathrm{s}$ for $\mu^*_\Sigma = \mu^{*,\lambda}_\Sigma$.

Empirical studies by Clift et al. [61, Fig 2.5] suggest a terminal Reynolds number of $Re_d = |\boldsymbol{u}|_r\, \rho_o\, d_0/\mu_o \approx 20.5 - 21.0$ for a bubble with $Eo_d = 40$ and $Mo = 0.056$ in a domain of infinite extend, which represents a Froude number of $Fr_d = |\boldsymbol{u}_r|/\sqrt{d_0\, g} \approx 0.626 - 0.642$ with respect to the chosen fluid properties and $Fr_d \approx 0.601 - 0.616$ considering the finite width of the applied computational domain. Denner et al. [44] reported a terminal Froude number of $Fr_d = 0.58$ using a VOF-PLIC method in a domain of $5d_0$ width and Pivello et al. [60] obtained a terminal Froude number $Fr_d = 0.606$ using a front-tracking method and a domain of $8d_0$ width.

Fig. 8a shows the temporal evolution of the Froude number $Fr_d$. The additional viscous dissipation imposed by $\mu^{*,t}_\Sigma = 0.07\,\mathrm{Pa\,s}$, Eq. (16), causes only a very small difference in the Froude number (*i.e.* rise velocity) of the bubble compared to the case without interface viscosity. Calculating the interface viscosity $\mu^{*,\lambda}_\Sigma = 0.6085\,\mathrm{Pa\,s}$ based on Eq. (19), on the other hand, results in a noticeably affected Froude number, which is particularly visible in the magnification of Fig. 8a. Despite the observed differences as a result of the artificial viscosity model and corresponding interface viscosity, the Froude numbers for all three cases are well within the expected range of Froude numbers as given by empirical studies and numerical results discussed in the previous paragraph. The total kinetic energy $E_{\mathrm{kin}}$ of the flow in the entire computational do-

**Table 1**
Values of $\mu^*_\Sigma$ and $\mu^*_\Sigma/\mu$ for different simulation time-steps $\Delta t$. Based on Eq. (2), $\Delta t_\sigma \simeq 3.4 \times 10^{-6}$ s.

| Fig. | 11a | 12a | 13a | 11b | 12b | 13b | 11c | 12c | 13c | 11d | 12d | 13d |
|---|---|---|---|---|---|---|---|---|---|---|---|---|
| $\Delta t$ ($\times 10^{-6}$ s) | 0.5 | | | 1.0 | | | 3.4 | | | 6.8 | | |
| $\Delta t/\Delta t_\sigma$ | 0.15 | | | 0.29 | | | 1.0 | | | 2.0 | | |
| $\mu^*_\Sigma$ ($\times 10^{-3}$ Pa s) | 0.0 | 1.46 | 2.92 | 0.0 | 2.92 | 5.84 | 0.0 | 9.93 | 19.9 | 0.0 | 19.9 | 39.8 |
| $\mu^*_\Sigma/\mu$ | 0.0 | 1.62 | 3.24 | 0.0 | 3.24 | 6.48 | 0.0 | 11.0 | 22.1 | 0.0 | 22.1 | 44.2 |
| $\Delta t_\mu$ ($\times 10^{-6}$ s) | $\infty$ | 463.2 | 213.6 | $\infty$ | 213.6 | 106.3 | $\infty$ | 56.72 | 28.22 | $\infty$ | 28.22 | 14.11 |

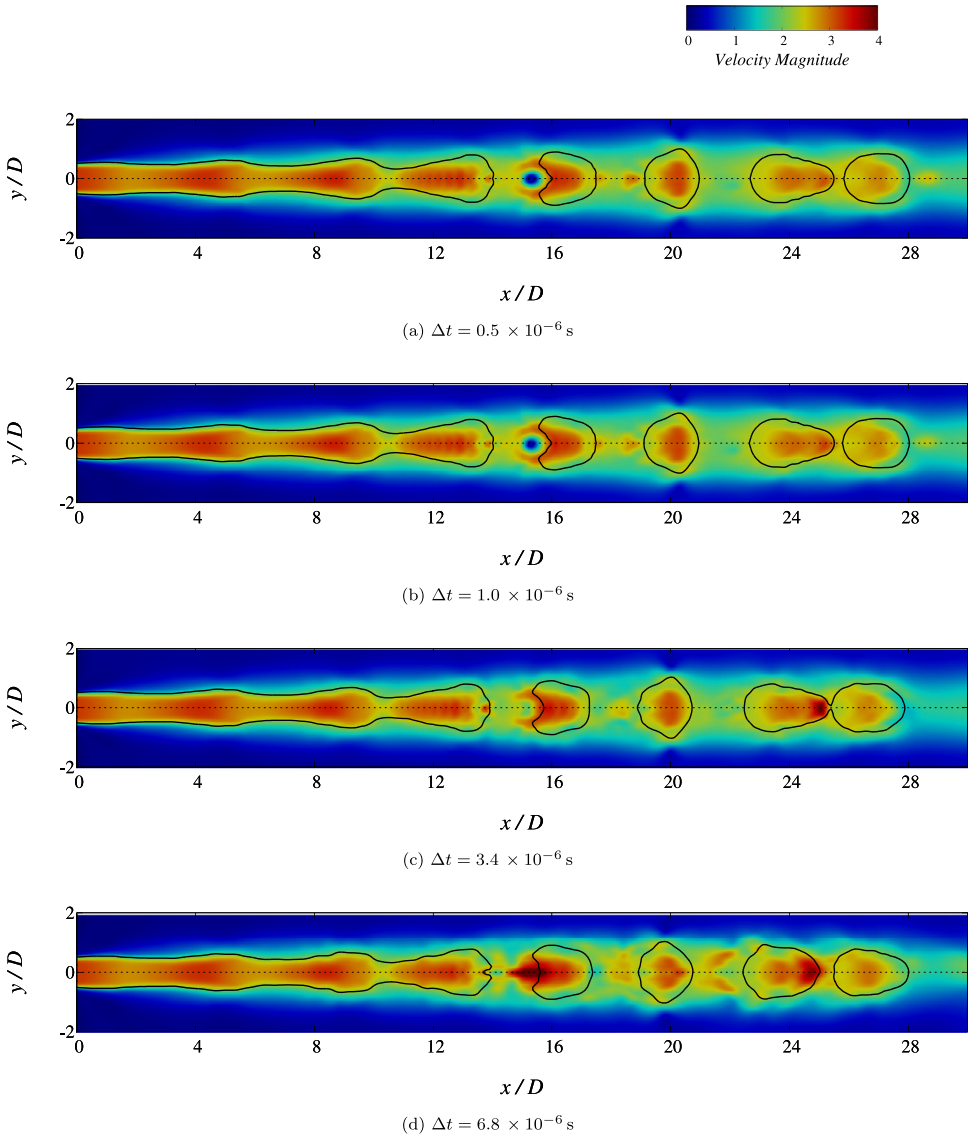


(a) $\Delta t = 0.5 \times 10^{-6}$ s

(b) $\Delta t = 1.0 \times 10^{-6}$ s

(c) $\Delta t = 3.4 \times 10^{-6}$ s

(d) $\Delta t = 6.8 \times 10^{-6}$ s

**Fig. 11.** Pulsed water jet at $t = 3.06 \times 10^{-3}$ s with $\mu^*_\Sigma = 0$ and for $\Delta t \in \{0.5, 1.0, 3.4, 6.8\} \times 10^{-6}$ s.

main exhibits a decreasing total kinetic energy in the domain for increasing interface viscosity as a results of the increased viscous dissipation, as seen in Fig. 8b.

### 5.4. Capillary instability of a liquid jet

The capillary instability of a water jet, schematically illustrated in Fig. 9, is simulated and analysed in order to assess the influence of the proposed artifical viscosity model on the prediction of the breakup length of the jet when the capillary time-step contraint is breached. Following the properties used by Moallemi et al. [62], the liquid phase has a density of $\rho = 9.97 \times 10^2$ kg m$^{-3}$ and a viscosity of $\mu = 9.0 \times 10^{-4}$ Pa s, whereas the gas phase has a density of $\rho_g = 1.18$ kg m$^{-3}$ and a viscosity of $\mu_g = 1.85 \times 10^{-5}$ Pa s. The liquid jet has a diameter of $d_o = 2r_o = 0.25$ mm and axial velocity $U_o = 3.0$ m s$^{-1}$, with a surface tension coefficient of $\sigma = 7.3 \times 10^{-2}$ N m$^{-1}$. This corresponds to a Weber number of $We = \rho\, r_o U_o^2/\sigma = 15.365$ and an Ohnesorge number of $Oh = \mu/\sqrt{\rho\,\sigma\, r_o} = 9.44 \times 10^{-3}$. A gravitational acceleration of $g = 9.81$ m s$^{-2}$ is acting in the positive $x$-direction. The applied computational domain is of size $40d_o \times 4d_o \times 4d_o$ and is resolved with an equidistant Cartesian mesh of $400 \times 40 \times 40$ cells. The liquid jet is initialised as a cylinder with a diameter $d_o$ and velocity $U_o$, the gas phase is initially at rest. Finally, the $x_0$ boundary is considered to be an inlet boundary, the $x_1$ boundary is considered to be a pressure outlet boundary, and all other boundaries are outlets.

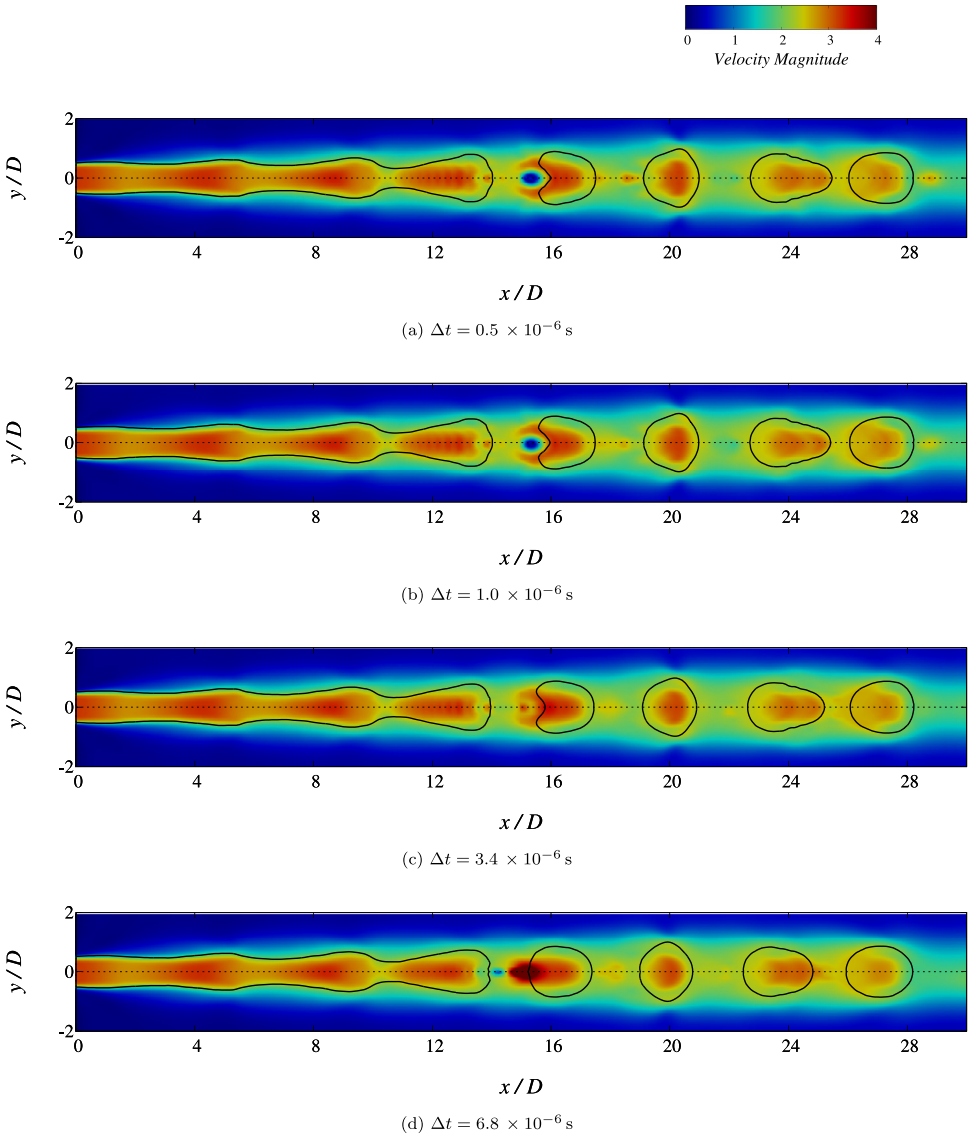


**Fig. 12.** Pulsed water jet at $t = 3.06 \times 10^{-3}$ s with $\mu_\Sigma^* = \mu_\Sigma^{*,t}$ and for $\Delta t \in \{0.5, 1.0, 3.4, 6.8\} \times 10^{-6}$ s.

Considering the equations of motion for an inviscid fluid in a cylindrical coordinate system ($r$, $\theta$, $x$), Rayleigh [63] conducted a linear stability analysis on the jet radius $r$ under the assumption that

$$r(\theta, x, t) = r_o + \alpha_n \cos(n\theta)\cos(kx), \tag{31}$$

with $\alpha_n \ll r_o$, and showed[1] that the original equilibrium becomes unstable for $n = 0$ and for a reduced wavenumber $\kappa = kr_o$ such that $|\kappa| < 1$. In that case, the jet radius can be rewritten as

$$r(x, t) = r_o + \epsilon_o \, \mathrm{e}^{qt} \cos(kx) \; \forall\theta, \tag{32}$$

and the growth rate of the unstable radius disturbance $q$ is given by

$$q^2 = \frac{\sigma}{r_o^3 \, \rho} \frac{\kappa I_1(\kappa)}{I_o(\kappa)} (1 - \kappa^2), \tag{33}$$

where $I_n$ is the modified Bessel's function of the $n$-th order. The dimensionless disturbance growth rate

$$\omega = q \sqrt{\frac{r_o^3 \, \rho}{\sigma}} \tag{34}$$

reaches its maximum $\omega_{\max} \simeq 0.3433$ for $\kappa \simeq 0.697$ [63].

Assuming that the linear approximation remains valid until the jet breaks up, the theoretical breakup time $t_\mathrm{b}$ is obtained by calculating the time necessary for the radial disturbance $\epsilon = \epsilon_o \, \mathrm{e}^{qt}$ defined in Eq. (32) to reach $\epsilon = r_o$, which gives

$$t_\mathrm{b} = \frac{\ln(r_o/\epsilon_o)}{q} = \frac{\ln(1/\eta_o)}{q} \;, \tag{35}$$

where $\eta_o = \epsilon_o / r_o$ is the dimensionless amplitude of the radial disturbance. The breakup length $L_\mathrm{b}$ follows from the breakup time $t_\mathrm{b}$ as

$$L_\mathrm{b} = U_o \, t_\mathrm{b} = \frac{U_o \, \ln(1/\eta_o)}{q}. \tag{36}$$

In the cases considered in this study, the inlet jet radius remains constant and equal to $r_o$, while the inlet jet velocity periodically

[1] In fact, Plateau [64] first proved that a liquid jet is stable for all purely non-axisymmetric deformations, but unstable to axisymmetric modes with $|\kappa| < 1$ [*i.e.* modes whose wavelength $\lambda (= 2\pi \, r_o/\kappa) > 2\pi \, r_o$]. Rayleigh [63] added to Plateau's theory by describing the dynamics of the instability.

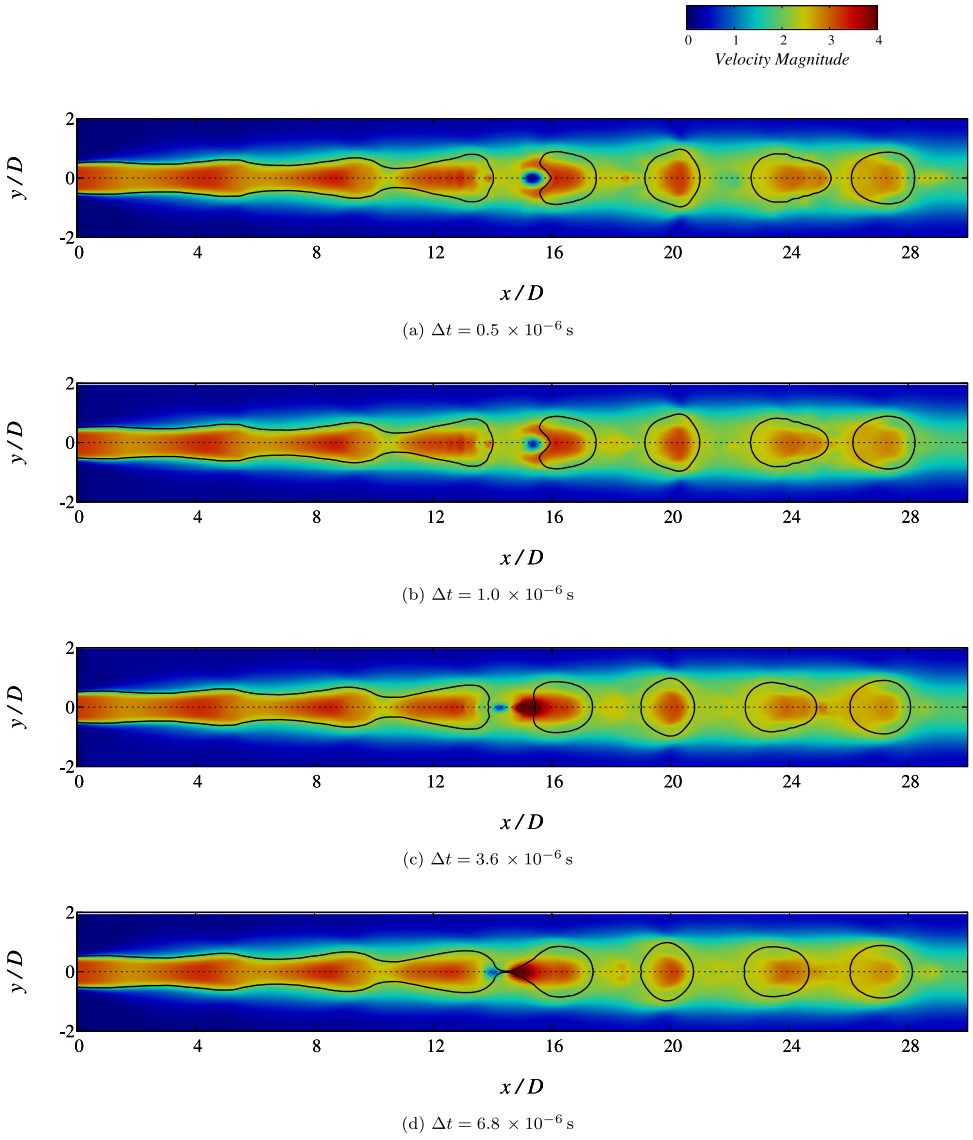


**Fig. 13.** Pulsed water jet at $t = 3.06 \times 10^{-3}$ s with $\mu^*_\Sigma = 2\mu^{*,t}_\Sigma$ and for $\Delta t \in \{0.5, 1.0, 3.4, 6.8\} \times 10^{-6}$ s.

changes with dimensionless amplitude $\xi_o$ following

$$U_{\text{inlet}} = U_o[1 + \xi_o \sin(\kappa\, U_o\, t/r_o)]. \tag{37}$$

Based on the mechanical energy of the perturbation, Moallemi et al. [62] derived a relationship between a radius perturbation $\eta_o$ and a velocity perturbation $\xi_o$, given as

$$\xi_o = \frac{2}{3}\eta_o. \tag{38}$$

Consequently, by inserting Eq. (38) in Eq. (36), the breakup length for a jet with a velocity perturbation $\xi_o$ becomes

$$L_{\text{b}} = \frac{U_o}{q}\ln\left(\frac{2}{3\,\xi_o}\right). \tag{39}$$

The liquid jet in the presented simulations is pulsed by a monochromatic perturbation imposed at the domain-inlet, periodically changing the mass flow with reduced wavenumber $\kappa = 0.7$ (to trigger the most unstable mode) and amplitude $\xi_o = 0.08$ from the mean. Based on the linear stability analysis of Rayleigh [63], the theoretical breakup length following from Eq. (39) with an initial amplitude of $\xi_o = 0.08$ is $L_{\text{b,R}} = 24.2\, r_o$.

Simulations are conducted for $\mu^*_\Sigma \in \{0, \mu^{*,t}_\Sigma, 2\mu^{*,t}_\Sigma\}$ using different numerical time-steps $\Delta t$, see Table 1. The interface viscosity $\mu^{*,t}_\Sigma$ (or a multiple thereof), given in Eq. (16), is deemed to be the most adequate choice for the evaluation of the interface viscosity for the considered case, because of its dependency on the time-step $\Delta t$. Alternatively, the values for $\mu^*_\Sigma$ given in Table 1 could, of course, be applied explicitly. Fig. 10 shows the breakup length $L_{\text{b}}$ normalised by the breakup length obtained from linear stability analysis, $L_{\text{b,R}} = 24.2$, as a function of the simulation time-step for three values of $\mu^*_\Sigma$. The additional dissipation imposed by $\mu^*_\Sigma$ increases the breakup length. For the case with the largest time-step $\Delta t = 2\Delta t_\sigma = 6.8 \times 10^{-6}$ s and the highest interfacial viscosity $\mu^*_\Sigma = 2\mu^{*,t}_\Sigma = 44.2\mu$, the breakup length $L_{\text{b}}$ is approximately 11% higher than for the same case without interface viscosity. This observation stands in agreement to previous findings [65], which suggest that an increase in viscosity increases the breakup time and length. The artificial viscosity model dissipates energy at the interface, thereby reducing the capillary-driven instability. Note that a perfect agreement with the result of the linear stability analysis is, of course, not expected, due to the limiting assumptions of the linear stability analysis as well as the limitations imposed by the finite spatiotemporal resolution of the conducted simulations and the associated difficulties in predicting what is a singular breakup event in reality [66]. However, the presented results with $\mu^*_\Sigma = 0$

and $\Delta t < \Delta t_\sigma$ are in very good agreement with the results reported by Moallemi et al. [62] for a water jet with the same fluid properties and only marginally smaller jet velocity ($We = 14.8$ and $Oh = 9.44 \times 10^{-3}$) as considered here.

Figs. 11–13 show a slice of the computational domain at $t = 3.06 \times 10^{-3}$ s with the interface contour and the underlying velocity field for each of the considered time-steps and interface viscosities. As previously seen in Fig. 10, the breakup is delayed by the additional interface viscosity imposed through the artificial viscosity model. This can also be concluded from comparing Figs. 11d and 13d. In the case of $\mu_\Sigma^* = 0$ depicted in Fig. 11d, breaching the capillary time-step limit results in visible oscillations of the interface as well as the velocity field. These oscillations are absent if the artificial viscosity model is applied, *i.e.* $\mu_\Sigma^* > 0$, of which the results are shown in Figs. 12d and 13d. This is due to the artificial viscosity model damping the (spurious) capillary waves with the shortest wavelengths. In general, the artificial viscosity has a negligible influence on the overall accuracy of the solution for $\mu_\Sigma^* \lesssim 3\mu$, as for instance observed by comparing the velocity fields in Figs. 11a-b and 12a-b, and based on the results plotted in Fig. 10.

## 6. Conclusions

An artificial viscosity model to mitigate the impact of numerical artefacts at fluid interfaces has been presented and validated. The artificial viscosity model is based on the tangential Laplacian of the interfacial velocity and an appropriately chosen interface viscosity. To this effect, the proposed method belongs to the broad class of artificial viscosity models, which are already widely used in other branches of CFD and numerical heat and mass transfer, such as turbulent transsonic flows.

A comprehensive analysis of results for representative test cases have been presented to validate and scrutinise the proposed methodology. The presented results demonstrate that the major physical mechanism associated with the artificial viscosity model is an increased viscous dissipation in the vicinity of fluid interfaces and an ensuing reduction of surface energy, which acts preferably at small length scales. Applying the artificial viscosity model has been shown to allow to breach the capillary time-step constraint and reduce the adverse impact of parasitic currents. As long as the applied interface viscosity is chosen carefully, the artificial viscosity model is found to not affect the accuracy and overall predictive quality of the numerical solution in a noticeable way, while in many cases improving the accuracy of the results due to the mitigation of numerical artefacts. Although the capillary time-step constraint is more restrictive than the viscous time-step constraint for all presented cases, for certain cases, if for instance the applied mesh resolution is very high, the viscous time-step constraint can be more restrictive than the capillary time-step constraint. In such cases, an implicit implementation of the artifical viscosity model is advisable. Nevertheless, the presented results obtained with an explicit implementation of the artificial viscosity model demonstrate the overall efficacy, which is not dependent on the type of implementation, of the proposed model.

Based on the presented results, the interface viscosity derived from the previous work of Raessi et al. [9], Eq. (16), performs generally better than the proposed interface viscosity based on the damping of capillary waves. This finding corresponds well with the convenient properties of the interface viscosity as defined by Eq. (16), as the interface viscosity generally increases under condition which typically lead to larger parasitic currents or faster capillary waves. The proposed interface viscosity derived from the damping of capillary waves, see Eq. (19), was found to provide typically too much damping in its current form. Nevertheless, it provides an alternative framework for the definition of the interface viscosity.

Following the extensive analysis presented for the dispersion of capillary waves, the evolution of long-wave instabilities on falling liquid films, the buoyancy-driven rise of a bubble and the capillary-driven breakup of a liquid jet, it can be concluded that for an interface viscosity of $\mu_\Sigma \lesssim 3\mu$ the impact on the accuracy of the results is negligible. However, dependent on the particular case, higher interfacial viscosities may be applicable without distorting the result in a significant manner. For instance, in the presented case of the long-wave instabilities on falling liquid films the applied interface viscosity $\mu_\Sigma \approx 23\mu$ prevents the onset of aliasing if the capillary time-step constraint is breached, while the influence of the artificial viscosity model on the evolution of the long-wave instability is insignificant despite the high interfacial viscosity. This can be explained by the long wave length of the examined interfacial waves in this case.

## Acknowledgements

The authors are grateful to the Engineering and Physical Sciences Research Council (EPSRC) for their financial support through grant EP/M021556/1 and to PETROBRAS for their financial support. Data supporting this publication can be obtained from https://doi.org/10.5281/zenodo.166716 under a Creative Commons Attribution license.

## References

[1] Brackbill J, Kothe D, Zemach C. Continuum method for modeling surface tension. J Comput Phys 1992;100:335–54.
[2] Williams MW, Kothe DB, Puckett EG. Accuracy and convergence of continuum surface-tension models. In: Shyy W, Narayanan R, editors. Fluid dynamics at interfaces. Cambridge University Press, Cambridge; 1999. p. 294–305.
[3] Cummins S, Francois M, Kothe D. Estimating curvature from volume fractions. Comput Struct 2005;83:425–34.
[4] Francois M, Cummins S, Dendy E, Kothe DB, Sicilian J, Williams MW. A balanced-force algorithm for continuous and sharp interfacial surface tension models within a volume tracking framework. J Comput Phys 2006;213:141–73.
[5] Mencinger J, Žun I. On the finite volume discretization of discontinuous body force field on collocated grid: application to VOF method. J Comput Phys 2007;221:524–38.
[6] Denner F, van Wachem B. Fully-coupled balanced-force VOF framework for arbitrary meshes with least-squares curvature evaluation from volume fractions. Numer Heat Transf Part B 2014;65:218–55.
[7] Abadie T, Aubin J, Legendre D. On the combined effects of surface tension force calculation and interface advection on spurious currents within volume of fluid and level set frameworks. J Comput Phys 2015;297:611–36.
[8] Hysing S. A new implicit surface tension implementation for interfacial flows. Int J Numer Methods Fluids 2006;51:659–72.
[9] Raessi M, Bussmann M, Mostaghimi J. A semi-implicit finite volume implementation of the CSF method for treating surface tension in interfacial flows. Int J Numer Methods Fluids 2009;59:1093–110.
[10] Sussman M, Ohta M. A stable and efficient method for treating surface tension in incompressible two-phase flow. SIAM J Sci Comput 2009;31:2447–71.
[11] Schroeder C, Zheng W, Fedkiw R. Semi-implicit surface tension formulation with a Lagrangian surface mesh on an Eulerian simulation grid. J Comput Phys 2012;231:2092–115.
[12] Zheng W, Zhu B, Kim B, Fedkiw R. A new incompressibility discretization for a hybrid particle MAC grid representation with surface tension. J Comput Phys 2015;280:96–142.
[13] Denner F, van Wachem B. Numerical time-step restrictions as a result of capillary waves. J Comput Phys 2015;285:24–40.
[14] Renardy Y, Renardy M. PROST: a parabolic reconstruction of surface tension for the volume-of-fluid method. J Comput Phys 2002;183:400–21.
[15] Fedkiw RP. A non-oscillatoryEulerian approach to interfaces in multimaterial flows (the Ghost Fluid method). J Comput Phys 1999;152:457–92.
[16] Kang M, Fedkiw RP, Liu XD. A boundary condition capturing method for multiphase incompressible flow. J Sci Comput 2000;15:323–60.
[17] Unverdi SO, Tryggvason G. A front-tracking method for viscous, incompressible, multi-fluid flows. J Comput Phys 1992;100:25–37.
[18] Popinet S. An accurate adaptive solver for surface-tension-driven interfacial flows. J Comput Phys 2009;228:5838–66.
[19] Zahedi S, Kronbichler M, Kreiss G. Spurious currents in finite element based level set methods for two-phase flow. Int J Numer Methods Fluids 2012;69:1433–56.
[20] Sussman M. A method for overcoming the surface tension time step constraint in multiphase flows II. Int J Numer Methods Fluids 2012:1343–61.
[21] Owkes M, Desjardins O. A mesh-decoupled height function method for computing interface curvature. J Comput Phys 2014;281:285–300.

[22] Coquerelle M, Glockner S. A fourth-order accurate curvature computation in a level set framework for two-phase flows subjected to surface tension forces. J Comput Phys 2016;305:838–76.
[23] Lamb H. Hydrodynamics. 6th ed. Cambridge University Press; 1932.
[24] Hirt CW, Nichols BD. Volume of fluid (VOF) method for the dynamics of free boundaries. J Comput Phys 1981;39:201–25.
[25] Osher S, Sethian JA. Fronts propagating with curvature-dependent speed: algorithms based on the Hamilton-Jacobi formulation. J Comput Phys 1988;79:12–49.
[26] Sussman M, Smereka P, Osher S. A level set approach for computing solutions to incompressible two-phase flow. J Comput Phys 1994;114:146–59.
[27] Harten A. High resolution schemes for hyperbolic conservation laws. J Comput Phys 1983;49:357–93.
[28] Sweby PK. High resolution schemes using flux limiters for hyperbolic conservation laws. SIAM J Numer Anal 1984;21:995–1011.
[29] Denner F, van Wachem B. TVD differencing on three-dimensional unstructured meshes with monotonicity-preserving correction of mesh skewness. J Comput Phys 2015;298:466–79.
[30] Osher S, Chakravarthy S. High resolution schemes and the entropy condition. SIAM J Numer Anal 1984;21:955–84.
[31] LeVeque R. Finite volume methods for hyperbolic problems. Cambridge University Press; 2002.
[32] von Neumann J, Richtmyer R. A method for the numerical calculation of hydrodynamic shocks. J Appl Phys 1950;21:232–7.
[33] Turkel E, Vatsa VN. Effect of artificial viscosity on three-dimensional flow solutions. AIAA J 1994;32:39–45.
[34] Caramana E, Shashkov M, Whalen P. Formulations of artificial viscosity for multi-dimensional shock wave computations. J Comput Phys 1998;144:70–97.
[35] Cook A, Cabot W. A high-wavenumber viscosity for high-resolution numerical methods. J Comput Phys 2004;195:594–601.
[36] Fiorina B, Lele SK. An artificial nonlinear diffusivity method for supersonic reacting flows with shocks. J Comput Phys 2007;222:246–64.
[37] Mattsson A, Rider W. Artificial viscosity: back to the basics. Int J Numer Methods Fluids 2015;77:400–17.
[38] Davis SF. A simplified TVD finite difference scheme via artificial viscosity. SIAM J Sci Stat Comput 1987;8:1–18.
[39] Levich V, Krylov V. Surface-tension-driven phenomena. Annu Rev Fluid Mech 1969;1:293–316.
[40] Denner F. Balanced-force two-phase flow modelling on unstructured and adaptive meshes. Imperial College London; 2013. Ph.D. thesis, http://hdl.handle.net/10044/1/28101.
[41] Balay S, Brown J, Buschelman K, Eijkhout V, Gropp WD, Kaushik D, et al. PETSc users manual; 2011.
[42] Balay S, Gropp WD, McInnes LC, Smith BF. Efficient management of parallelism in object oriented numerical software libraries. In: Arge E, Bruasat A, Langtangen H, editors. Modern software tools in scientific computing. Birkhaeuser Press; 1997. p. 163–202.
[43] Denner F, van Wachem B. Compressive VOF method with skewness correction to capture sharp interfaces on arbitrary meshes. J Comput Phys 2014;279:127–44.
[44] Denner F, van der Heul D, Oud G, Villar M, da Silveira Neto A, van Wachem B. Comparative study of mass-conserving interface capturing frameworks for two-phase flows with surface tension. Int J Multiphase Flow 2014;61:37–47.
[45] Denner F, van Wachem B. On the convolution of fluid properties and surface force for interface capturing methods. Int J Multiphase Flow 2013;54:61–4.
[46] Bänsch E. Finite element discretization of the Navier-Stokes equations with a free capillary surface. Numerische Mathematik 2001;88:203–35.
[47] Scriven L. Dynamics of a fluid interface: equation of motion for Newtonian surface fluids. Chem Eng Sci 1960;12:98–108.
[48] Denner F. Frequency dispersion of small-amplitude capillary waves in viscous fluids. Phys Rev E 2016;94:023110.
[49] Prosperetti A. Viscous effects on small-amplitude surface waves. Phys Fluids 1976;19:195–203.
[50] Deike L, Berhanu M, Falcon E. Energy flux measurement from the dissipated energy in capillary wave turbulence. Phys RevE 2014;89:023003.
[51] Prosperetti A. Motion of two superposed viscous fluids. Phys Fluids 1981;24:1217–23.
[52] Kalliadasis S, Ruyer-Quil C, Scheid B, Velarde M. Falling liquid films. Applied mathematical sciences, 176. Springer Verlag, London; 2012.
[53] Kelly R, Goussis D, Lin S, Hsu F. The mechanism for surface wave instability in film flow down an inclined plane. Phys Fluids A 1989;1:819–28.
[54] Nosoko T, Miyara A. The evolution and subsequent dynamics of waves on a vertically falling liquid film. Phys Fluids 2004;16:1118–26.
[55] Denner F, Pradas M, Charogiannis A, Markides C, van Wachem B, Kalliadasis S. Self-similarity of solitary waves on inertia-dominated falling liquid films. Phys Rev E 2016;93:033121.
[56] Denner F., Charogiannis A., Pradas M., Markides C., van Wachem B., Kalliadasis S. Solitary waves on falling liquid films in the drag-inertia regime: computations and experiments. Submitted to Journal of Fluid Mechanics 2015.
[57] Charogiannis A, An J, Markides C. A simultaneous laser-induced fluorescence, particle image velocimetry and particle tracking velocimetry technique for the investigation of liquid film flows. Exp Therm Fluid Sci 2015;68:516–36.
[58] Pradas M, Tseluiko D, Kalliadasis S. Rigorous coherent-structure theory for falling liquid films : viscous dispersion effects on bound-state formation and self-organizationRigorous coherent-structure theory for falling liquid films : viscous dispersion effects on bound-state formation and self-organization. Phys Fluids 2011;23:044104.
[59] Nosoko T, Yoshimura P, Nagata T, Oyakawa K. Characteristics of two-dimensional waves on a falling liquid film. Chem Eng Sci 1996;51:725–32.
[60] Pivello M, Villar M, Serfaty R, Roma A, Silveira-Neto A. A fully adaptive front tracking method for the simulation of two phase flows. Int J Multiphase Flow 2014;58:72–82.
[61] Clift R, Grace J, Weber M. Bubbles, drops and particles. New York: Academic Press; 1978.
[62] Moallemi N, Li R, Mehravaran K. Breakup of capillary jets with different disturbances. PhysFluids 2016;28:012101.
[63] Rayleigh L. On the capillary phenomena of jets. Proc R Soc London 1879;29:71–97.
[64] Plateau J. Statique expérimentale et théorique des liquides soumis aux seules forces moléculaires, 2. Gauthier-Villars; 1873.
[65] Chandrasekhar S. Hydrodynamic and hydromagnetic stability. Clarendon Press Oxford, England; 1961.
[66] Castrejón-Pita J, Castrejón-Pita A, Thete S, Sambath K, Hutchings I, Hinch J, et al. Plethora of transitions during breakup of liquid filaments. Proc. Natl. Acad. Sci. U.S.A. 2015;112:4582–7.